J Nanopart Res (2014) 16:2622
DOI 10.1007/s11051-014-2622-9

RESEARCH PAPER

Investigating the effects of particle size and chemical structure on cytotoxicity and bacteriostatic potential of nano hydroxyapatite/chitosan/silica and nano hydroxyapatite/chitosan/silver; as antibacterial bone substitutes

Shima Tavakol · Mohammad Reza Nikpour · Elham Hoveizi · Behnaz Tavakol · Seyed Mahdi Rezayat · Mahdi Adabi · Sahebeh Shajari Abokheili · Mohsen Jahanshahi

Received: 13 May 2014 / Accepted: 21 August 2014 / Published online: 2 September 2014

Abstract The restoration of defective bone tissue and complications related to surgery and fracture site infection are major concerns in orthopedic surgeries. However, it is crucial to develop osteoconductive and bacteriostatic composites. Chitosan/nano hydroxyapatite (CT/n-HAp) powder containing of Ag and Si were prepared by an in situ hybridization method. The aim of this work was to elucidate the effect of size, surface roughness, and chemical structure of mentioned nanocomposites on cytotoxicity and bacteriostatic activity via human osteoblast cells and Escherichia Coli, respectively. Particle size, surface roughness, reactive oxygen specious production, and bioactivity of nanocomposites were investigated by X ray diffraction, atomic force microscopy, DPPH assay, and SEM/UV–Visible spectrophotometer, respectively. Bacterial colony counting test, MTT assay and lactate dehydrogenase (LDH) release were performed as bacteriostatic and biocompatibility tests. The results showed that CT/n-HAp/Ag with smaller particle size in the range of 1–22.6 nm (10.00 ± 0.09 nm) than CT/n-HAp/Si in the range

S. Tavakol (✉) · S. M. Rezayat · M. Adabi
Department of Medical Nanotechnology, School of Advanced Technologies in Medicine, Tehran University of Medical Sciences, Tehran, Iran
e-mail: sh_tavakol@razi.tums.ac.ir

S. Tavakol
Student's Scientific Research Center, Tehran University of Medical Sciences, Tehran, Iran

S. Tavakol
School of Medicine, Razi Institute for Drug Research, Iran University of Medical Sciences, Tehran, Iran

M. R. Nikpour (✉) · M. Jahanshahi (✉)
Nanobiotechnology Research Group, Nanobiotechnology Research Department, Nanotechnology Research Institute, Babol University of Technology, P.O.BOX: 484- 47144, Babol, Iran
e-mail: rezanikpour16@yahoo.com

M. Jahanshahi
e-mail: mjahan@nit.ac.ir

E. Hoveizi
Department of Biology, Faculty of Sciences, Shahid Chamran University, Ahvaz, Iran

B. Tavakol
Department of Medicine, School of Medicine, Kashan University of Medical Sciences, Kashan, Iran

S. Shajari Abokheili
Faculty of Chemical Engineering–Polymer Branch, Azad University of Shiraz, Shiraz, Iran

of 3–72.5 nm (18.00 ± 0.14 nm) exhibits higher cell viability and bacteriostatic activity, and less LDH release from cell plasma membrane. Integration of Ag into the nanocomposite hindered the release of Ag^+ ions and restricts cytotoxic potential on cells. Higher cytotoxic effect of CT/n-HAp/Si might be related to proton concentration derived from nanocomposite and its chemical structure. In conclusion, the strong bone regeneration potential of CT/n-HAp and good biocompatibility and bacteriostatic activity of CT/n-HAp/Ag make it as potential bacteriostatic bone filler in site of infected bone fracture.

Keywords Nano hydroxyapatite · Tri-phasic nanocomposite · Particle size · Silver · Bacteriostatic · Biocompatibility · Nanomedicine

Introduction

A serious concern in orthopedic is the threat of osteomyelitis and infections associated with fracture in the site of surgery and diabetic patients. The incidence of pediatric osteomyelitis is between 2.9 and 75/100,000 individuals (Stoesser et al. 2013) in which antibacterial therapy and surgical intervention has been supposed. The development of new bone repairing material has recently focused on the osteoconductivity (Tavakol et al. 2013a), biocompatibility and bacteriostatic activities of the materials. The structure of bone consisting of two main phases at the nanoscale level including collagen nanofiber and hydroxyapatite nano particles (n-HAp) is an amazing nanocomposite. Due to its superior biocompatibility, bioactivity and osteoconductivity potential (Tan et al. 2012), n-HAp is an appealing biomaterial with potentials for bone substitute (Sionkowska and Kozłowska 2010), dental (Sadat-Shojai et al. 2010), and maxillofacial applications (Notodihardjo et al. 2012). Our earlier study showed that chitosan/nanohydroxyapatite (CT/n-HAp) caused higher bone regeneration, in vitro and in vivo (Tavakol et al. 2013b). So, in this study we investigated the cytotoxic and bacteriostatic potential of addition of poly dimethyl siloxan (Si) and silver (Ag) material to this nanocomposite as bone filler in site of infected bone fractures.

Owing to high surface area-to-volume-ratio, n-HAp has received considerable attention from the biologists and biomaterial scientists and has been extensively applied in bone fillers (Luo et al. 2011), coating of orthopedic implants (Roy et al. 2011) and stem cell-culture (Muzzarelli 2011). In comparison with pure HAp, polymeric nanocomposites have shown improved mechanical properties, such as modulus, strength and stiffness (Albano et al. 2011; Wagoner Johnson and Herschler 2011). Particulate HAp has the disadvantage of implant site movement and potentially causes damage to healthy tissues. To resolve this clinical problem, nanocomposite materials composed of HAp and natural (Tavakol et al. 2012, 2013b) or synthetic (Murugan and Rao 2003) polymers have been developed. The advantages of these systems depend on the combination of functional properties of single phase materials. Natural polymer-based composites obtained from collagen (Itoh et al. 2002), alginate (Murugan and Panduranga Rao 2002), gelatin (Tavakol et al. 2012), chitosan (CT) (Tavakol et al. 2013a), silica (Heinemann et al. 2011), and etc. (Pang and Zhitomirsky 2008) are playing a significant role in a variety of tissue engineering applications because of their tailor-made physical, chemical, mechanical, and biological characteristics.

Chitosan, an *N*-deacetylation product of chitin can support the growth, function and cellular activity of osteoblasts and chondrocytes. Furthermore, CT is used in the design of environmentally responsive biomaterials as it has exhibited a great biocompatibility, biodegradability, and bioactivity in human's body (Khanna et al. 2010; Tavakol et al. 2013a). The mechanical reliability and in vivo biomineralization of CT/HAp nanocomposites have shown to be superior compared to those of either HAp or CT alone (Yamaguchi et al. 2001; Tavakol et al. 2013a).

In addition, CT has a high metal binding efficacy, especially with Ag. Metallic nanoparticles such as copper, zinc, and Ag with low concentration are widely used in medicine as antimicrobial agents. In mammals, the high concentrations can cause cytotoxicity and argyria (Kim et al. 2010; Sahithi et al. 2010). According to the experimental observations (Miyaji et al. 2005; Zyman et al. 2006), the use of the ammonium and nitrate precursors may cause the defects in HAp structure due to the incorporation of $NH4^+$ and $NO3^-$ ions into the HAp. Ammonia with Ag ions, in alkaline pH conditions, builds a very stable complex ion $[Ag\ (NH3)_2]^+$ that can affect the amount of Ag to be included into HAp (Thompson and Kateley 1999). Other researchers reported the combination of Ag with HAp as the uniform formation of Ag in HAp/CT

together (Pang and Zhitomirsky 2008; Saravanan et al. 2011). As an example, the nano-silver (n-Ag) in the poly (vinyl pyrrolidone) composite is found to have a significant antibacterial effect against bacteria (Hwang and Jeong 2011). Several in vitro studies reported that the Ag ions in the HAp coatings play an important role in preventing or minimizing the initial bacterial adhesion (Chen et al. 2006, 2007; Mo et al. 2008). However, recent study demonstrated the role of n-Ag in bone regeneration (Hui et al. 2014).

Siloxan is currently receiving attention for biomedical applications as a substitute for Ca in the crystal network of HAp and tri-calcium phosphate (Best et al. 2008; Botelho et al. 2006). Additionally, not only does Si play an essential role in metabolic events, but it also leads to endochondral and intramembranous bone formation (Carlisle 1980a, b). This component with Ca, Na, and P acts on the expression of certain genes responsible for controlling the cell cycle of animal, human osteoblasts and stimulates osteo-production. In addition, there were several attempts to introduce Si into a HAp network. The formation of nanocomposites containing HAp and Si in a CT matrix is an effective way to improve the bioactivity level of the material (Best et al. 2008; Thian et al. 2006a, b; Jongwattanapisan et al. 2011).

The aim of this study was to investigate the effects of size, surface roughness, and chemical structure of CT/n-HAp/Ag and CT/n-HAp/Si as a bone substitute biomaterial in spine fracture and craniofacial application on biocompatibility (eukaryote (human osteoblast cell)) and bacteriostatic potential of prokaryote cells (*Escherichia coli (E-Coli)).* Since, *E. Coli* is one of the causes of osteomyelitis; it was selected in this study (Giovanardi 2014). The morphology and the structural property of the products before and after being soaked into bovine serum albumin (BSA) were investigated by SEM and FTIR analyses, respectively. In eukaryotic cytotoxicity study, lactate dehydrogenase (LDH) release and MTT assays were assessed. The LDH release test is related to damage to cytoplasm plasma membrane facing the nanocomposite, but MTT assay demonstrated damage to mitochondria

Materials and methods

Chemicals materials

Chitosan (obtained from crab shells with $a > 85$ % degree of deacetylation), $AgNO_3$ and Poly (dimethyl siloxane) (PDMS) were purchased from Sigma-Aldrich Co. Acetic acid (HAc, 99.8 %) was obtained from Merck. Poly (ethylene glycol) (PEG) with moderate molecular weight of 400, was used to control the particle growth during precipitation, Cetyltrimethylammonium bromide (CTAB) as a moisturizing agent, Calcium nitrate tetrahidrate ($Ca(NO_3)_2 4H_2O$), Diammonium hydrogen phosphate ($(NH_4)_2HPO_4$), sodium hydroxide (NaOH) and BSA were all supplied by Merck, Germany.

Nutrients and materials including peptone water, meat extract, and agar powder required for bacteriological experiments were purchased from HIMEDIA. *E. Coli* (PTCC 1763) was obtained from Iranian Research Organization for Science and Technology. Human osteoblast cells were a gift from Pasteur institute.

Synthesis of CT/n-HAp nanocomposite

Chitosan was dissolved in 100 cc 2 % (v/v) acetic acid solution to obtain a polymer solution by way of made CT/n-HAp solution from the previous report (Tavakol et al. 2013a). Solution was taken in such amount that Ca/P molar ratio was maintained at 1.67. Then $Ca(NO_3)_2 4H_2O$ of 0.5 M solution was added in CT solution and vigorously stirred at room temperature with a mechanical stirrer (2,500 rpm). Subsequently, $(NH_4)_2HPO_4$ suspension of 0.5 M was added drop wise into the prior mixture under extreme stirred until the better suspension was achieved. Stirring was continued up for another 24 h to obtain a homogeneous polymer solution. The resulting solution was held unstirred for another night to remove the air bubbles trapped in viscous liquid. In whole process, the pH value was adjusted to about 11 using 2 M NaOH solution and the reaction temperature was kept at 25 °C. Finally the white gelatinous precipitate was separated by centrifugation the suspension at 3,000 rpm for 30 min (Z-36HK Hermle, Germany). Then the mixture was dried in a freeze-dryer (FDE-0350, Korea) at −50 °C for 48 h to make powder.

Synthesis of CT/n-HAp/Si nanocomposite

The CT/n-HAp/Si tri-component nanocomposite was prepared by an in situ hybridization method. As prepared CT/n-HAp solution from the previous report (Tavakol et al. 2013a) was used in synthesis of tri-component nanocomposite. First, the PDMS was gently

added to the pre-prepared dispersion and the mixture was vigorously agitated with mechanical stirring at about 1,000 rpm for 4 h at room temperature. Stirring was continued for overnight at room temperature with a hard mechanical stirrer to obtain a homogeneous viscous solution. The resulting solution was held unstirred for another night so that the air bubbles trapped in viscous liquid could be removed. Finally, the gelatinous precipitate was separated by centrifuging the suspension at 4,500 rpm for 45 min (Z-36HK Hermle, Germany). Subsequently, the gel fraction of the mixture was dried in a freeze-dryer (FDE-0350, Korea) at −50 °C for 48 h. In the whole process, the pH value was adjusted to be about 11 using 2 M NaOH solution and the reaction temperature was kept at room temperature.

Synthesis of CT/n-HAp/Ag nanocomposite

Like the CT/n-HAp/Si nanocomposite, the CT/n-HAp/Ag was also prepared by an in situ hybridization technique and the prepared CT/n-HAp solution was used in this nanocomposite. To prepare the tri-phasic nanocomposite consisting of Ag, 2 gr of CT powder was dissolved into 100 ml of distilled water containing acetic acid and kept on constant stirring until a clear viscous solution was obtained. In the next step, the $AgNO_3$ suspension of 0.5 M was added drop wise to the prepared solution and the precursor with high speed stirring overnight to obtain a homogenous dispersion. To prevent clay formation in solution, the pH value was adjusted to about 7, using 2 M NaOH solution at room temperature. The combination of pH range and a mechanical agitation of the mixture during gelation were conducted in order to prevent the formation of a bulk gel. The resulting solution was kept unstirred for another night to remove the trapped air bubbles in viscous liquid. Finally, the prepared gelatinous precipitated component was separated by centrifuging the suspension at 4,500 rpm for 45 min (Z-36HK Hermle, Germany). The mixture was lyophilized in a freeze-dryer (FDE-0350, Korea) at −50 °C for 48 h until it dried and the powder was obtained. Ag concentration was calculated to be 7.2 ppm.

Characterization

X-ray diffraction and FTIR analysis

The crystal structure and the powders phase were both analyzed with X-ray diffraction (XRD) (Equinox3000, INEL France) under the voltage and current settings of 40 kV and 30 mA, respectively, and Cu Ka radiation (1.5405 Å). For qualitative analysis, XRD diagrams were recorded in the interval $20° \leq 2\theta \leq 45°$ at the scan rate of 2°/min. The mean crystallite sizes "D" were determined according to the Scherrer Equation, $D = 0.9\lambda/\beta \cos\theta$, where D is the average crystallite size in Å, β is the peak broadening of the diffraction line measured at half of its maximum intensity in "adian", λ is the wavelength of X-rays, and θ is the Bragg's diffraction angle. The chemical structures of obtained products were determined by FTIR spectrum. The FTIR analysis (Perkin Elmer, USA) was undertaken within the scanning range of 400–4,000 cm^{-1}.

Atomic force microscopy (AFM) and scanning electron microscopy (SEM) study

The surface roughness, morphology, dispersion, and size distribution of synthesized powders were shown using a JEOL6330F field emission AFM. For better examination and particle size distribution, 2D and 3D pictures of the samples were also provided based on AFM analysis.

SEM (VEGAII TESCAN) was used to characterize the morphology and surface roughness of the synthesized nanocomposite materials before and after soaking in BSA. Prior to imaging, the products mounted on aluminum stubs that were gold coated to increase conductivity.

Bioactivity assessment

Bovine serum albumin with a concentration of 20 mg/ml was primed as simulated body fluid. BSA is commonly used to simulate human albumin since it is very similar to it in its sequence of amino acid units. Synthesized powder samples were immersed in a BSA solution. The solution was kept for 7 days and then dried at room temperature. The soaking and protein adsorption effect of the immersed powders in BSA were then investigated by FTIR, SEM micrograph (VEGAII TESCAN) and spectrophotometer (in 595 nm, by JENWAY 63.5 UV/VIS spectrophotometer, UK).

Antibacterial assays

Two different kinds of antibacterial tests were carried out to investigate the antibacterial potential of

synthesized CT/n-HAp/Ag and CT/n-HAp/Si nanocomposites against *E. coli* as a sample of gram negative bacteria.

Inhibition zone test

The inhibition zone experiment was used to show the bacteriostatic capability of prepared samples. 1 gr of each synthesized powder was shaped as a 17-mm disk-like piece using homemade pressing device operating at 10 bars. The media were autoclaved and inoculated with a fresh seed culture where the size of inoculums was 5 % (v/v). All the samples were also irradiated with ultra violet (UV) radiation for 30 min to ensure sterility. Agar plate was prepared by autoclaving the liquid media (containing 8 wt% Agar) and was allowed to cool down in petri-dish which was previously sterilized. 3 gr/l peptone water and 5 gr/l meat extract were added to *E. coli*. Diluted *E. coli* was spiked on agar plate and incubated at 37 °C overnight. Disk-like samples were placed on *E. Coli* spiked agar plates overnight and then, were photographed by a digital camera.

Colony counting test

The liquid medium was prepared as described in the previous Sect. 1 gr of each synthesized powders were incubated with 10 ml of *E. coli* suspension in autoclaved test tubes. *E. coli* content of the initial suspension was measured to be 3.2 × 109 cfu/ml by serially diluting the suspension with sterilized water. After 24 h of incubation, 100 µl of each suspension was used to measure the bacterial content with the aforesaid procedure.

Diphenyl-2-picryl-hydrazyl (DPPH) assay

DPPH with an unpaired valence electron has free radical scavenger potential and was applied as antioxidant assay. Since acidic environment affects this assay, methanol was added to neutralize pH and capture protons. Based on this data, the pH of samples might be indirectly investigated. DPPH (Sigma-Aldrich, USA) was diluted in methanol (100 µM). The extract of nanocomposites was prepared in the first, third, 8th, and 14th days of incubation in deionized water. 100 µM solution of DPPH in methanol was added to pure extracts and methanol diluted extracts in the ratio of ½ for pH neutralizing. They were kept in 30 °C for 30 min, and the absorbance was measured using Eliza reader at 517 nm (Fisher Lifesciences).

MTT assay

MTT assay was done to compare the cell viability of human osteoblast cells which were treated on the third day of powders extraction. The extracts of powders were prepared in poor Ca^{2+} and Mg^{2+} HANKS'S media on the third days post-incubation. Human osteoblast cells were a gift from Pasteur Institute of Iran, Tehran, Iran. Briefly, human osteoblast cells were isolated from human three molar and purified by direct antifibroblast labeling and MACS microbeads. Isolated cells have been analyzed using immunocytochemistry (anti-OB cadherin, and antifibroblast surface protein) and alkaline phosphates production. The data approved isolation of human osteoblast cell with high purity (Shokrgozar et al. 2010). Human osteoblast cells were seeded on 96 well plates for 24 h, then extracts were added for 24 h incubation period. 3-(4,5-dimethylthiazol-2-yl)-2,5 diphenyltetrazolium bromide was added for 4 h, and then DMSO was added to dissolve the insoluble purple formazan product into a colored solution. Absorbance was read at 570 nm using ELIZA reader (Fisher Life sciences). All samples were analyzed in triplicate. Data were normalized with CT/n-HAp.

LDH release

The extracts from the 1st, 3rd, 8th, 14th, 21st days, were applied for LDH release test (Roche). They were added on the seeded osteoblast cells with above mentioned medium overnight. Afterward, 100 µl/well of supernatant was transferred into corresponding wells and 100 µl/well reaction mixtures was added and incubated 30 min at 25 °C. Absorbance was read at 490 nm in 96-well format using ELIZA reader (Fisher Lifesciences). All samples were analyzed in triplicate.

Statistical analysis

The Graph pad software was applied to calculate and analyze reactive oxygen specious (ROS) production, bioactivity, colony counting, cell viability and LDH

release data using t student tests. $P < 0.05$ was found statistically significant. In this study CT/nHAp was used as a benchmark; however, data have not been shown.

Results

Crystal structure and chemical analysis

Figure 1a shows the X-ray diffraction patterns of the synthesized nanocomposites. For nanoparticles, the existence of peaks at 2θ of approximately 21.2°, 23°, 26°, 28.3°, and 32.5° corresponds to the diffraction planes of the crystallites, respectively, and therefore confirmed the formation and presence of two component nanocomposites referring to the calcium hydrogen phosphate shape. The existence of special peaks at 2θ of approximately 21°, 29°, 33.4°, 37°, and 42.5° which are attributed to Ag^{+} ions confirms the existence of $[Ag(NH_3)_2]^{+}$ This is possibly the reason for the compression originated from the contracting polymeric matrix through interfacial bonding. Mean crystallite size was calculated using Scherer's equation in which the approximate crystallite sizes of synthesized samples were found to be about 8.6 and 7.2 nm for CT/n-HAp/Si and CT/n-HAp/Ag, respectively.

Size distribution and surface roughness analysis

AFM was applied to evaluate the particle size distributions and surface roughness of nanocomposites. The size distribution results for the CT/n-HAp/Si and CT/n-HAp/Ag nanocomposites were in the ranges of 3–72.5 and 1–22.6 nm with a mean size of 18.00 ± 0.14 and 10.00 ± 0.09 nm, respectively (Fig. 1b).

The surface topography and the surface properties of nanocomposites in 2D and 3D topographies are shown in Fig. 1c. The results revealed that the nanoparticles surfaces consisting of Ag had higher surface roughness than surfaces containing Si. It was clearly seen that these particles had better dispersion in the matrix solution.

Chemical structure before and after immersion

Figure 2a and b. displays the FTIR spectra of nanocomposite samples before and after immersion in BSA. The absorption bands observed around 2,917, 1,642, 1,456, and 1,552 cm^{-1} were assigned to methylene (CH_2), amide I (C=O), amino (NH_2), and amide II (–NH). The absorption bands observed at around 1,099, 952, 839, and 563 cm^{-1} correspond to a phosphate group, while the stretching band (approximately

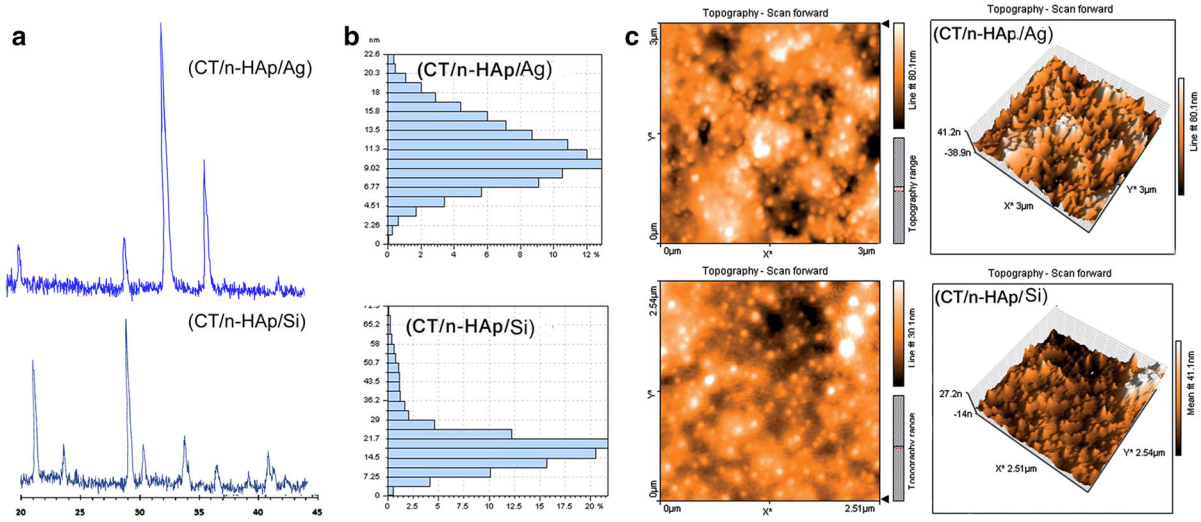

Fig. 1 **a** XRD Pattern of the CT/nHA nanocomposite containing of Si and Ag prepared by an in situ hybridization method. **b** Size distribution of the nanocomposite containing Si and Ag by AFM indicated mean size of 18 ± 0.14 and 10 ± 0.09 nm, respectively. **c** AFM images of the nanocomposite surface imaged in tapping-mode in air indicated CT/nHA/Ag had higher surface roughness than surfaces containing Si

between 2,900 and 3,700 cm^{-1}) was assigned to OH group set. Also, carbonate bands at about 1,457, 1,433, and 840 cm^{-1} were observed. The feature bands for $HPO4^{2-}$ were determined approximately at 1,131, 1,062, 988, 876, 576 and 528 cm^{-1}. It seems that the magnitude of these bands become weaker after adding Si and Ag content which is attributed to the development of in situ hybridization method. Furthermore, characteristic bands for $PO4^{3-}$ appeared at 963 cm^{-1}. More significantly, new band appearing at 880 cm^{-1} for CT/n-HAp/Si sample is assigned to Si–O vibration modes of $SiO4^{4-}$ groups. Additionally, another new band appearing at 820 cm^{-1} for CT/n-HAp/Si tri-component is related to Si–O–Si vibration modes of polymerized $SiO4^{4-}$ groups. From an overall comparison of the FTIR analysis for the different samples, the effective existence of HAp nanoparticles surrounded at nanocomposites was confirmed in all of them, the characteristic absorption bands of carbonated-HA were observed.

Morphological studies

Figure 3Aa and b shows the SEM micrographs of fracture surface of the nanocomposite samples. According to the obtained results, it is shown that HAp particles in nanocomposites were covered with a continuous smooth CT layer and the HAp and the Si and the Ag particles were homogenously distributed within the uniform CT matrix. It can be said that the Ag and Si nanoparticles, which were surrounded and embedded into the CT polymer chain, had a core effect on the polymerization of nanocomposites.

Bioactivity assessment

The synthesized samples were soaked in BSA solution for 7 days to evaluate their bioactivity (Fig. 3Ac and d). These figures show that after the soaking, the surface of particles was covered with a layer assumed to be newly formed apatite. It is understood that not only are the surfaces of the soaked samples entirely covered with these apatite layers, they are also in accordance with the FTIR observation of the samples after immersion (Fig. 2b). It appears in the same time interval CT/n-HAp/Si caused more apatite layer on the surface than CT/n-HAp/Ag. In other words, CT/n-HAp/Si made higher bioactivity than other nanocomposite (Fig. 3B).

Antibacterial testing

The bacteriostatic potential of prepared samples has been shown in Fig. 4a. The bacteriostatic potential of synthesized nanocomposites against *E. Coli* was evaluated by the zone of inhibition and it was observed that inhibition zone of CT/n-HAp/Ag was larger than other nanocomposite.

Since disk diffusion test is a qualitative experiment, the effect of prepared nanocomposites against *E. coli*, colony counting experiment was done in a quantitative study. As reported in Fig. 4c, bacterial content of different media containing nanocomposites was measured by serial dilution method. These results clearly showed that CT/n-HAp/Ag sample significantly exhibited higher bacteriostatic potential against *E. coli* than CT/n-HAp/Si. The two-tailed *P* value was 0.0071, considered very significant.

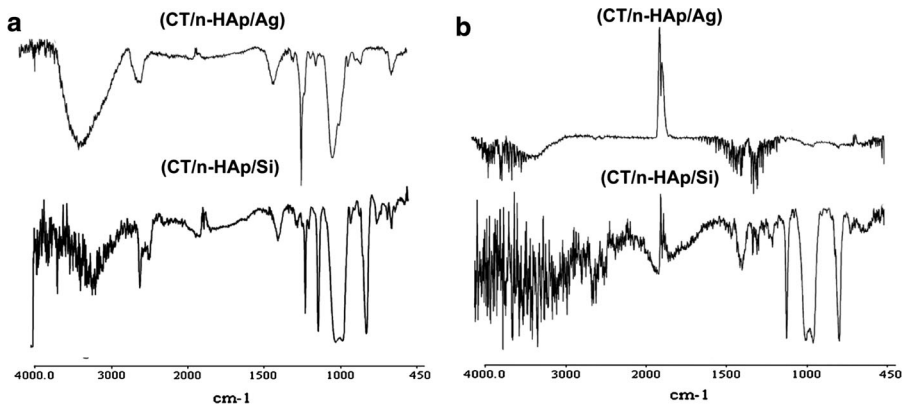

Fig. 2 **a** FTIR spectra of the nanocomposites before soaking in BSA. **b** FTIR spectrum of nanocomposite after soaking in BSA

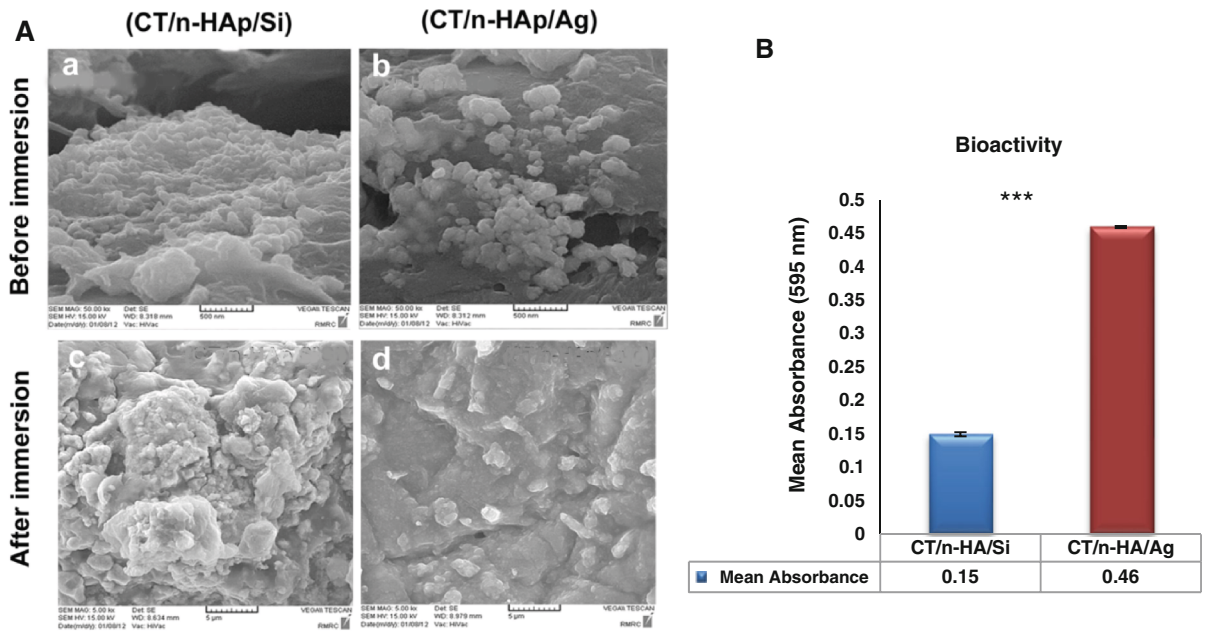

Fig. 3 **A***a* and **A***b*, SEM images of the nanocomposites before soaking in BSA. **A***c* and **A***d*, SEM images of the nanocomposites after soaking in BSA, **B**) Mean absorbance of the BSA treated by CT/nHA/Ag and CT/nHA/Si. ***P value < 0.0001 and the difference was extremely significant

Determination of free radical scavenger property

To measure ROS production, DPPH assay was done. The decrease of absorbance is directly proportional to the ROS production. The results showed that CT/n-HAp/Ag and CT/n-HAp/Si exhibited no ROS production (Fig. 5a). Figure 5b showed that CT/n-HAp/Si produced significantly higher acidic values as compared to CT/n-HAp/Ag (P value was <0.001). However, there was no significant difference between proton concentrations of samples at different time periods in CT/n-HAp/Si.

MTT assay

The cell viability of the prepared cell-seeded nanocomposites was analyzed by MTT reduction; cell viability is directly proportional to the formazan production. The results showed that there was significant difference between viability of human osteoblast cells treated by CT/n-HAp/Ag as compared to CT/n-HAp/Si. CT/n-HAp/Ag significantly induced higher cell viability as compared to other ones (P value was <0.01) (Fig. 5c) and both of them induced higher cell proliferation than CT/n-HAp.

LDH activity

The LDH activity test was done to measure the cytotoxic potential of soluble substances. The LDH production is directly proportional to damage to the plasma membrane of cell. There was a significant difference observed to plasma membrane damage of human osteoblast cells treated by nanocomposites at different times. CT/n-HAp/Ag significantly induced less LDH release from cell plasma membrane as compared to CT/n-HAp/Si and control group in all of the time periods. In the other words, CT/n-HAp/Ag induced no damage to cell plasma membrane; however CT/n-HAp/Si induced significantly cell plasma membrane damage as compared to control and CT/n-HAp/Ag at 3rd and 14th days of extraction. But at the first, 8th and 21st days of extraction showed LDH release comparable to the control group (Fig. 5d).

Discussion

In this study, an in situ hybridization method was used to make of the CT/n-HAp/Ag and the CT/n-HAp/Si.

Fig. 4 **a** and **b** bacteriostatic potential of the nanocomposites against *E. Coli* by the inhibition zone test. **c** Bacterial content of different media containing nanocomposites by serial delusion method. *Yellow line* showed negative control. ***P* value lower than 0.0071, considered very significant difference. (Color figure online)

CT/n-HAp/Ag had a smaller size than the other nanocomposite, and exhibited higher human osteoblast cell viability and bacteriostatic activity as well as less cytotoxicity LDH release. It seems that Ag particles were trapped into CT/n-HAp/Ag and inhibited burst release of Ag^{+}, and prevented adverse effect of these ions on the cell plasma membrane. Finally, owing to its smaller particle size (10 nm), nanocomposite passes directly through the plasma membrane and exhibits no cell plasma membrane damage. However, in the CT/n-HAp/Si, ROS production might be one of the explanations for higher LDH release and cell mortality. Whether CT/n-HAp/Si in the range of 10 nm induces equal bacteriostatic effects compared to CT/n-HAp/Ag awaits future studies. Regarding our data, CT/n-HAp/Ag can be served as a good substitute in infected bone problems.

Autologous bone grafting is a gold standard in bone defect but osteomyelitis treatment has remained one of the most obstacles in orthopedic. So, design of a bone substitute material that can control osteomyelitis is a great desire (Pape et al. 2010). The main point of this study was to evaluate the effect of surface morphology, size distribution, and chemical structure of materials on cytotoxicity and bacteriostatic activities of biodegradable CT/HAp nanocomposites consisting of Ag and Si. As shown in Fig. 1a, the Si and the Ag substitution had no significant effect on diffraction pattern. The small changes in the crystal structure are resulted from the incorporation of a slightly larger silicate ion in the region of phosphate ions, and the strong molecular interactions between HAp, CT, and Si contents. Moreover, the increase in the Si content caused a slight decrease in the loss of some OH groups (Figs. 1a, 2a), and led to a small modification in the crystalline size of the nanocomposite which this is in agreement with Fig. 1b. The shift and a decrease in the intensity of each peak in the CT/n-HAp/n-Ag and CT/n-Hap/Si after composite formation might be attributed to molecular interactions between Ag and matrix. Since protons and metal ions compete to bind to amine groups of CT, and pH value plays an important role in binding metal ions. Considering the use of acidic CT solutions for the deposition, the amino groups of CT become positively charged because of the protonation, which makes it difficult to form Ag^{+} ion chelate to CT (Pang and Zhitomirsky 2008). Hence, less acidic environment favors the binding of metal ions to amine groups of CT.

Comparison of FTIR spectra in different samples confirmed existence of HAp nanoparticles surrounding the nanocomposites, and it can be concluded that all possess the characteristic absorption bands of carbonated-HAp. These results showed that, after the creation of tri-composites, the OH broad band in samples became weaker and even decreased as the water adsorptions reduced after the formation of nanocomposites. Also, it was revealed that, with the addition of third components, the peak for the amide I band of CT shifted toward smaller wave numbers. The displacement number was about 33 cm^{-1} (from 1,623.03 to 1,590.38 cm^{-1}), which indicates a strong interaction between CT and the additional component. It is also inferred that the inductive effect is caused by

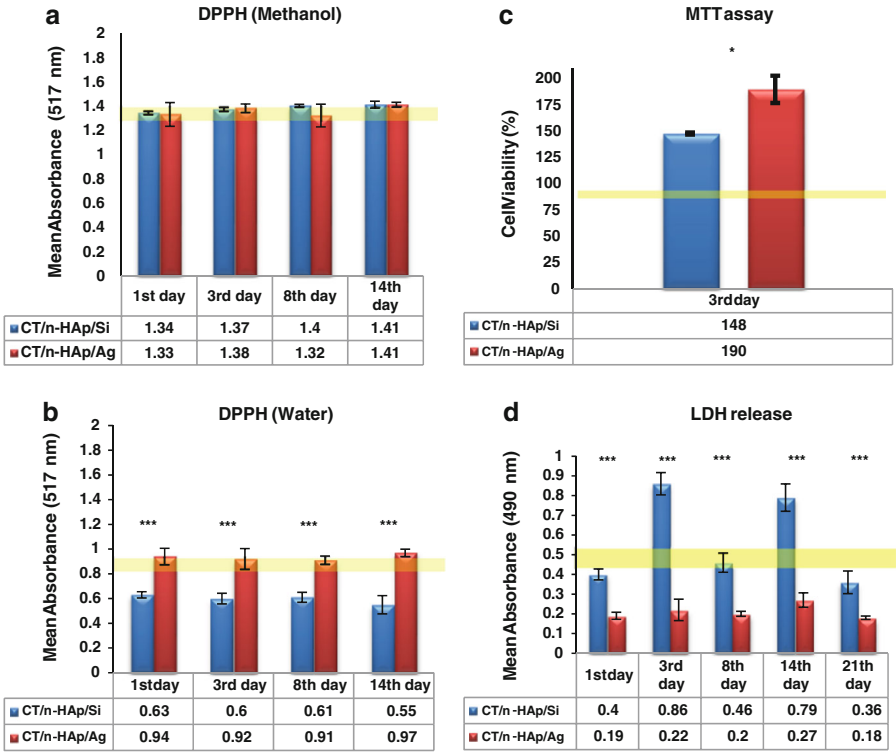

Fig. 5 **a** Measurement of ROS production of the nanocomposites using DPPH test. *Yellow line* showed negative control and *purple line* showed DPPH alone. **b** Indirectly shows proton concentrations of nanocomposite extract. *Yellow line* showed negative control and purple line showed DPPH alone. *** Means the difference was extremely significant ($P < 0.0001$). **c** Cell viability of the human osteoblast cells measured by MTT assay. *Yellow line* showed n-HAp/CT group. * Means difference was significant ($P < 0.5$) **d** Cell membrane damage of hEnSC treated by nanocomposites was measured by LDH assay. *Yellow line* showed negative control. *** The difference was extremely significant ($P < 0.0001$). (Color figure online)

the coordination interaction between NH_2 groups of the CT, and thus Ag ions lead to a shift in the peaks.

SEM showed that the NPs exhibit spherical inorganic minerals dispersed within the polymeric matrix, and surface roughness of the nanocomposite increased by addition of Ag and few elliptic aggregations were found on the surface of these nanocomposites. It seems that surface modification of these products is enhanced by the suitable solubility of the NPs in the organic solvents, and also prevents further agglomeration in particles.

Also, the AFM images give the impression that the existence of Ag and Si increased surface roughness. These micrographs are in good accordance with the SEM images that showed the presence of agglomerations among the particles, which might be the result of interface binding between dispersed particles and matrix. The enhancement in interfacial binding leads to a highly specific surface energy of particles and the matrix aggregations. The SEM results showed that the surface consisting of Ag had better dispersion in the matrix solution, which resulted in smaller particle size of CT/n-HAp/Ag. It can be concluded that the particle size of nanocomposites is controlled by the biopolymer matrix in nanocomposites as depicted in the AFM micrographs.

After 7 days of nanocomposites soaking in BSA, a dense and homogenous form of calcium phosphate on the surface of samples were observed, which could also be seen in the SEM as well as the FTIR images (Figs. 3Ac, d and 2a). It was seen that all of the peaks in the FTIR spectrum remained after soaking. However, the intensity of peaks decreased and compressed. However, the intensity of phosphate and carbonate group peaks increased in comparison to other peaks because of the formation of apatite-like layer. In these samples there were many n-HAp which could act as nucleation sites. Notably, the OH broad peak was eliminated after soaking. The loss of this group would be possibly due to the incorporation of HAp in the

polymer structure. In the same time interval it appears that because of the ceramic structural of the tri-component sample, CT/n-HAp/Si has eventually induced more apatite layer on the surface.

Surface roughness, particle size, proton concentration and chemical structure of nanocomposite powders influenced bioactivity, cell viability, plasma cell membrane damage and bacteriostatic potential. Based on the results, CT/n-HAp/Ag induced lower bioactivity, cell lethality, plasma cell membrane damage and higher bacteriostatic activity than CT/n-HAp/Si.

As mentioned in the results of bacteriostatic analysis, the addition of Ag induced higher bacteriostatic activity (Fig. 4). Based on earlier studies, the antibacterial properties significantly differed with the use of different metals, and also the effectiveness of metals to resist bacterial attachment is different with the bacterial strain.

High bacteriostatic activity of CT/n-HAp/Ag might be the result of particles size, Ag^+ ions and intercellular ROS production. The size of particles determines the type of cell lethality and bacteriostatic activity. In our study, the size of nanocomposite containing Ag was 10 nm, and studies have reported that the mode of toxicity in Ag particles smaller than 10 nm are more related to Ag^+ ion, and NPs may directly pass through the cell membrane, but in the larger ones, particle-cell interaction is dominated (Choi and Hu 2008). On the other hand, mammalian cells would uptake calcium phosphate nanoparticles by endocytosis together with the Ag cargo, and after lysosomal degradation, Ag ions release into the cell. Therefore, one of the important factors in bacteriostatic activity of this nanocomposite will be Ag^+ ions. As smaller n-Ag particles have higher surface/volume, they more oxidizes silver layer on the surface, thus results in more Ag^+ ions in the solution (Pratsinis et al. 2013).

However, the positive Ag^+ ions can be adsorbed to the negative charge of plasma membrane, and target and kill bacterial cells. There are different proposed mechanisms of bacterial killing: they can bind to the microbial DNA and prevent bacterial replication or to sulfhydryl groups of bacterial enzymes and inhibit cellular respiration, or bind to vital molecules transporter across the cell membrane and within the cells and disrupt its action (Chen et al. 2006). Choi and Hu (2008) indicated that the effect of n-Ag on bacterial growth is size-dependent. They realized n-Ag <5 nm was more toxic against bacteria than larger ones, and n-Ag can pass through cell membrane, accumulate in the cell and cause cell malfunction due to their small size. Moreover, Lok et al. (2006) proved that n-Ag which has attached to the cell membrane, can change membrane permeability and cause cell death. Similar results were reported by Morones et al. (2005), who found the average size of n-Ag able to penetrate into *E. Coli* membrane, was about 5 nm.

Another important factor is intracellular ROS production. Since there was no compromise in the integrity of plasma membrane in nanocomposite containing Ag, it can be said that cell lethality and bacteriostatic activity was related to intracellular ROS production. However, this nanocomposite did not produce extracellular ROS. Intracellular ROS might be produced owing to passing of Ag^+ ions through transmembrane or even direct internalization of small NPs to cytoplasm and lysosome. Intracellular Ag^+ ions will be produced because of the acidic pH in the lysosome, and the triggering of cell death via apoptosis through the activation of cyt-c. It might be said that, eventually, direct traveling of NPs to cytoplasm was a more important key factor than the production of Ag^+ ions in medium and the transfer of these ions through transmembrane. According to the MTT assay data and low cell viability, it might be postulated that the reason can be related to the fast formation of Ag^+ ions due to contact of oxidized silver layer with solution.

Significant LDH release and cell mortality of nanocomposite containing Si might be related to high concentration of proton and acidic environment derived from nanocomposite. Further studies are recommended for this postulation. MTT assay and LDH data were in good agreement to eachothers and proton concentration. The LDH results revealed that the CT/n-HAp/Si posed greater damage to the cell plasma membrane compared to other nanocomposite. It might be said that higher level of proton concentration derived from CT/n-HAp/Si has induced higher cell plasma membrane damage than other ones.

High bacteriostatic activity of CT/n-HAp/Si might be attributed to the size of particles, SiO_2 formation, high bioactivity and proton concentration.

It has been shown that greater surface area and more active sites, as well as higher surface/volume ratio induces more cytotoxicity effects on the cells, and smaller mesoporous silicon particles have higher

cytotoxicity (Santos et al. 2010). A key factor why the bactericidal activity and cell viability of CT/n-HAp/Si were less than nanocomposite containing of Ag, might be due to surface chemistry of the CT/n-HAp/Si particles. Another factor is formation of intracellular ROS due to proton concentration in the presence of Si particles at smaller particle sizes.

A recent report addressed the production of ROS, where hamster ovary mutant cells were cultured on soaked crystalline-Si membranes for 60 days, inducing mitochondrial injury and DNA breakage (Jiang et al. 2009). Moreover, mitochondrial oxidative stress can be originated from the loss of mitochondrial scavenging capacity, or by an increase in the antioxidant mechanism of the cells by producing ROS (Batandier et al. 2002).

Bioactivity might be another influential factor in the increase of bacteriostatic activity of this nanocomposite. It is reasonable to state that the binding of the NPs to the bacteria depends on the interaction of the surface area available and biofilm formation. However, the bacteriostatic mechanism of CT/n-HAp/Si might be related to its high bioactivity, so as to adsorb more bacteria. This is because of the fact that oxidized silicon layer on the surface and proton concentration might damage the bacterial cell membrane, or even pass through the transmembrane, and induce ROS production (Bhattacharjee et al. 2010).

Acknowledgments This work was supported by grant from Student's Scientific Research Center, Tehran University of Medical Sciences, Tehran, Iran.

References

Albano C, Perera R, Cataño L, Karam A, González G (2011) Prediction of mechanical properties of composites of HDPE/HA/EAA. J Mech Behav Biomed 4(3):467–475

Batandier C, Fontaine E, Kériel C, Leverve XM (2002) Determination of mitochondrial reactive oxygen species: methodological aspects. J Cell Mol Med 6(2):175–187

Best S, Zou S, Brooks RA, Huang J, Rushton N, Bonfield W (2008) The osteogenic behaviour of silicon substituted hydroxyapatite. Key Eng Mat 361:985–988

Bhattacharjee S, de Haan LH, Evers NM, Jiang X, Marcelis AT, Zuilhof H et al (2010) Role of surface charge and oxidative stress in cytotoxicity of organic monolayer-coated silicon nanoparticles towards macrophage NR8383 cells. Part Fibre Toxicol 7(1):25

Botelho C, Brooks R, Best S, Lopes M, Santos J, Rushton N et al (2006) Human osteoblast response to silicon-substituted hydroxyapatite. J Biomed Mater Res A 79:723–730

Carlisle EM (1980a) A silicon requirement for normal skull formation in chicks. J Nutr 110:352–359

Carlisle EM (1980b) Biochemical and morphological changes associated with long bone abnormalities in silicon deficiency. J Nutr 110:1046–1056

Chen W, Liu Y, Courtney HS, Bettenga M, Agrawal CM, Bumgardner JD et al (2006) In vitro anti-bacterial and biological properties of magnetron co-sputtered silver-containing hydroxyapatite coating. Biomaterials 27: 5512–5517

Chen W, Oh S, Ong A, Oh N, Liu Y, Courtney H et al (2007) Antibacterial and osteogenic properties of silver-containing hydroxyapatite coatings produced using a sol gel process. J Biomed Mater Res A 82(4):899–906

Choi O, Hu Z (2008) Size dependent and reactive oxygen species related nanosilver toxicity to nitrifying bacteria. Environ Sci Technol 42(12):4583–4588

Giovanardi D (2014) Cranial osteomyelitis due to *E. coli* infection in commercial layers. Vet Rec 18;174(3):76

Heinemann S, Coradin T, Worch H, Wiesmann H, Hanke T (2011) Possibilities and limitations of preparing silica/collagen/hydroxyapatite composite xerogels as load-bearing biomaterials. Compos Sci Technol 71(16):1873–1880

Hui Q, Chen Z, Zhiquan A, Yao J, Yaochao Z, Jiaxin W, Xin L, Bing H, Xianlong Z, Yang W (2014) Silver nanoparticles promote osteogenic differentiation of human urine-derived stem cells at noncytotoxic concentrations. Int J Nanomed 9:2469–2478

Hwang S, Jeong S (2011) Electrospun nano composites of poly (vinyl pyrrolidone)/nano-silver for antibacterial materials. J Nanosci Nanotechnol 11(1):610–613

Itoh S, Kikuchi M, Takakuda K, Nagaoka K, Koyama Y, Tanaka J et al (2002) Implantation study of a novel hydroxyapatite/collagen (HAp/col) composite into weight-bearing sites of dogs. J Biomed Mater Res 63(5):507–515

Jiang J, Huo K, Chen S, Xin Y, Xu Y, Wu Z (2009) Intracellular chromosome breaks on silicon surface. Biomaterials 30:2661–2665

Jongwattanapisan P, Charoenphandhu N, Krishnamra N, Thongbunchoo J, Tang I, Hoonsawat R et al (2011) In vitro study of the SBF and osteoblast-like cells on hydroxyapatite/chitosan–silica nanocomposite. Mater Sci Eng C 31:290–299

Khanna R, Katti KS, Katti DR (2010) In situ swelling behavior of chitosan–polygalacturonic acid/hydroxyapatite nanocomposites in cell culture media. Int J Polym Sci 1–12

Kim YS, Song MY, Park JD, Song KS, Ryu HR, Chung YH et al (2010) Subchronic oral toxicity of silver nanoparticles. Part Fibre Toxicol 7:20

Lok C-N, Ho C-M, Chen R, He Q-Y, Yu W-Y, Sun H et al (2006) Proteomic analysis of the mode of antibacterial action of silver nanoparticles. J Proteome Res 5(4): 916–924

Luo X, Zhang L, Morsi Y, Zou Q, Wang Y, Gao S et al (2011) Hydroxyapatite/polyamide 66 porous scaffold with an ethylene vinyl acetate surface layer used for simultaneous substitute and repair of articular cartilage and underlying bone. Appl Surf Sci 257(23):9888–9894

Miyaji F, Kono Y, Suyama Y (2005) Formation and structure of zinc-substituted calcium hydroxyapatite. Mater Res Bull 40(2):209–220

Mo A, Liao J, Xu W, Xian S, Li Y, Bai S (2008) Preparation and antibacterial effect of silver–hydroxyapatite/titania nanocomposite thin film on titanium. Appl Surf Sci 255(2): 435–438

Morones JR, Elechiguerra JL, Camacho A, Holt K, Kouri JB, Ramírez JT et al (2005) The bactericidal effect of silver nanoparticles. Nanotechnology 16(10):2346

Murugan R, Panduranga Rao K (2002) Biodegradable coralline hydroxyapatite composite-gel using natural alginate. Key Eng Mater 240:407–410

Murugan R, Rao KP (2003) Graft polymerization of glycidylmethacrylate onto coralline hydroxyapatite. J Biomater Sci Polym Ed 14(5):457–468

Muzzarelli R (2011) CT composites with inorganics, morphogenetic proteins and stem cells, for bone regeneration. Carbohydr Polym 83:1433–1445

Notodihardjo FZ, Kakudo N, Kushida S, Suzuki K, Kusumoto K (2012) "Bone regeneration with BMP-2 and hydroxyapatite in critical-size calvarial defects in rats. J Craniomaxillofac Surg 40(3):287–291

Pang X, Zhitomirsky I (2008) Electro deposition of hydroxyapatite–silver–CT nanocomposite coatings. Surf Coat Technol 202:3815–3821

Pape HC, Evans A, Kobbe P (2010) Autologous bone graft: properties and techniques. J Orthop Trauma 24:S36–S40

Pratsinis A, Hervella P, Leroux J-C, Pratsinis SE, Sotiriou GA (2013) Toxicity of silver nanoparticles in macrophages. Small 15:2576–2584

Roy M, Bandyopadhyay A, Bose S (2011) Induction plasma sprayed nano hydroxyapatite coatings on titanium for orthopaedic and dental implants. Surf Coat Technol 205(8):2785–2792

Sadat-Shojai M, Atai M, Nodehi A, Khanlar LN (2010) Hydroxyapatite nanorods as novel fillers for improving the properties of dental adhesives: synthesis and application. Dent Mater 26(5):471–482

Sahithi K, Swetha M, Prabaharan M, Moorthi A, Saranya N, Ramasamy K et al (2010) Synthesis and characterization of nanoscale hydroxyapatite-copper for antimicrobial activity towards bone tissue engineering applications. J Biomed Nanotechnol 6:333–339

Santos HA, Riikonen J et al (2010) In vitro cytotoxicity of porous silicon microparticles: effect of the particle concentration, surface chemistry and size. Acta Biomater 6(7):2721–2731

Saravanan S, Nethala S, Pattnaik S, Tripathi A, Moorthi A, Selvamurugan N (2011) Preparation, characterization and antimicrobial activity of a bio-composite scaffold containing chitosan/nano-hydroxyapatite/nano-silver for bone tissue engineering. Int J Biol Macromol 49(2):188–193

Shokrgozar M, Farokhi M, Rajaei F, Bagheri M, Azari S, Ghasemi I (2010) Biocompatibility evaluation of HDPE-UHMWPE reinforced β-TCP nanocomposites using highly purified human osteoblast cells. J Biomed Mater Res A 95:1074–1083

Sionkowska A, Kozłowska J (2010) Characterization of collagen/hydroxyapatite composite sponges as a potential bone substitute. Int J Biol Macromol 47(4):483–487

Stoesser N, Pocock J, Moore CE, Soeng S, Hor P, Sar P (2013) The epidemiology of pediatric bone and joint infections in Cambodia, 2007–11. J Trop Pediatr 59(1):36–42

Tan F, Naciri M, Dowling D, Al-Rubeai M (2012) In vitro and in vivo bioactivity of CoBlast hydroxyapatite coating and the effect of impaction on its osteoconductivity. Biotech adv 30(1):352–362

Tavakol S, Kashani IR, Azami M, Khoshzaban A, Tavakol B, Kharrazi S et al (2012) In vitro and in vivo investigations on bone regeneration potential of laminated hydroxyapatite/gelatin nanocomposite scaffold along with DBM. J Nanopart Res 14(12):1–14

Tavakol S, Khoshzaban A, Azami M, Kashani IR, Tavakol H, Yazdanifar M, Sorkhabadi SM (2013a) The effect of carrier type on bone regeneration of demineralized bone matrix in vivo. J Craniofac Surg 24(6):2135–2140

Tavakol S, Nikpour M, Amani A, Soltani M, Rabiee S, Rezayat S et al (2013b) Bone regeneration based on nanohydroxyapatite and hydroxyapatite/chitosan nanocomposites: an in vitro and in vivo comparative study. J Nanopart Res 15(1):1–16

Thian E, Huang J, Best S, Barber Z, Bonfield W (2006a) Silicon-substituted hydroxyapatite thin films: Effect of annealing temperature on coating stability and bioactivity. J Biomed Mater Res A 78:121–128

Thian ES, Huang J, Best SM, Barber ZH, Brooks RA, Rushton N et al (2006b) The response of osteoblasts to nanocrystalline silicon-substituted hydroxyapatite thin films. Biomaterials 27:2692–2698

Thompson ML, Kateley LJ (1999) The Nernst equation: determination of equilibrium constants for complex ions of silver. J Chem Educ 76(1):95

Wagoner Johnson AJ, Herschler BA (2011) A review of the mechanical behavior of CaP and CaP/polymer composites for applications in bone replacement and repair. Acta Biomater 7(1):16–30

Yamaguchi I, Tokuchi K et al (2001) Preparation and microstructure analysis of chitosan/hydroxyapatite nanocomposites. J Biomed Mater Res 55(1):20–27

Zyman Z, Rokhmistrov D, Ivanov I, Epple M (2006) The influence of foreign ions on the crystal lattice of hydroxyapatite upon heating. Mater Wiss Werkst Technol 37(6):530–532